Valley-resolved Fano resonance in monolayer transition metal dichalcogenide nanoribbons with attached stubs

Hui-Ying Mu,[1] Nie-Wei Wang,[1] Ying-Na Du,[1] Xing-Tao An,[1,2,*] and Jian-Jun Liu[3]

[1]*Hebei Provincial Key Laboratory of Photoelectric Control on Surface and Interface, School of Science, Hebei University of Science and Technology, Shijiazhuang, Hebei 050018, China*

[2]*Key Laboratory for Microstructural Material Physics of Hebei Province, School of Science, Yanshan University, Qinhuangdao 066004, China*

[3]*Physics Department, Shijiazhuang University, Shijiazhuang 050035, China*

(Received 9 November 2021; revised 11 March 2022; accepted 14 March 2022; published 24 March 2022)

Besides spin, the valley degree of freedom is also a promising candidate as a carrier of information. Spintronics has come a long way, and spin modulation can be realized by quantum interference and the spin-orbit coupling effect. However, how to control the valley degree of freedom using quantum interference is still a problem to be explored. Here, we discover a mechanism for producing valley polarization in a monolayer transition metal dichalcogenide nanoribbon with attached stubs, in which valley-resolved Fano resonance is formed due to the quantum interference of intervalley backscattering. When the quantum interference occurs between the localized states at the edge of the stubs and the continuous channels in the nanoribbon, the transmission dips of the Fano effect are valley polarized. As the number of stubs increases, the valley-polarized transmission dips will split, and valley-resolved minigaps are formed by Fano resonance with intervalley backscattering in the stub superlattice. When the electron incident energy is in these valley-resolved gaps of the superlattice, even with several stubs, the transmission can have a significant valley polarization. Our findings point to an opportunity to realize valley functionalities by quantum interference.

DOI: 10.1103/PhysRevB.105.115305

I. INTRODUCTION

Fano resonance arises from the quantum interference between two interfering configurations, one directly through the continuum states and the other through a discrete level [1]. The constructive and destructive interferences of the two configurations give rise to a characteristic asymmetric line shape in the spectrum. Although the Fano resonance is established in spectroscopy, it has been observed as a ubiquitous phenomenon in a wide variety of physical processes with coexisting discrete and continuum states, particularly electronic transport in a low-dimensional nanostructure [2–15]. Both experimental and theoretical investigations have indicated that Fano resonance has potential application in spintronics [7–10] and optoelectronics devices [16,17].

Fano resonance also occurs in monolayer materials, such as graphene and monolayer transition metal dichalcogenides (MTMDs) [6,11,18,19]. The energy dispersion of electrons in these materials usually has a pair of degenerate minima located at well-separated momentum space points, known as valleys. Besides spin, the valley degree of freedom also provides a feasible way to design information-storage or information-processing devices. Similar to the control of the spin polarization in spintronics, the manipulation of valley polarization configurations, i.e., unequal population distribution among the degenerate valleys, is one of the key elements for valleytronics devices. The valley polarization has been widely studied by using edges [20], doping [21], defects [22,23], lattice strains [24–28], intervalley scattering [29,30], or valley-dependent trigonal warping of the dispersions [31]. Meanwhile, the spinlike properties of the valley, including the valley Hall effect [32–34], the valley magnetic response [21,35–42], and the valley optical selection rules [43,44], allow its manipulation similar to the spin controls. A large spin polarization can be generated in semiconductor nanostructures that involves both the spin properties and the quantum interference effects related to spin-dependent Fano resonance. However, it is still a pertinent challenge to realize valley polarization in monolayer honeycomb lattice materials using valley quantum interference effects, such as valley-dependent Fano resonance.

Here, we discover that in a MTMD nanoribbon with an attached stub, the Fano resonance, i.e., the dip in the transmission spectrum caused by the quantum interference between the localized states of the stub and the continuum states in the nanoribbon, is split into two valley-resolved dips. This valley selectivity is made possible by the intervalley backscattering induced by the localized states in the stub. When the number of stubs attached to the nanoribbon increases, each valley-resolved Fano dip will further split into multiple dips. Therefore the valley-resolved minigaps will be formed for stub superlattice structures. A sizable valley polarization can

*Corresponding author: anxt2005@163.com

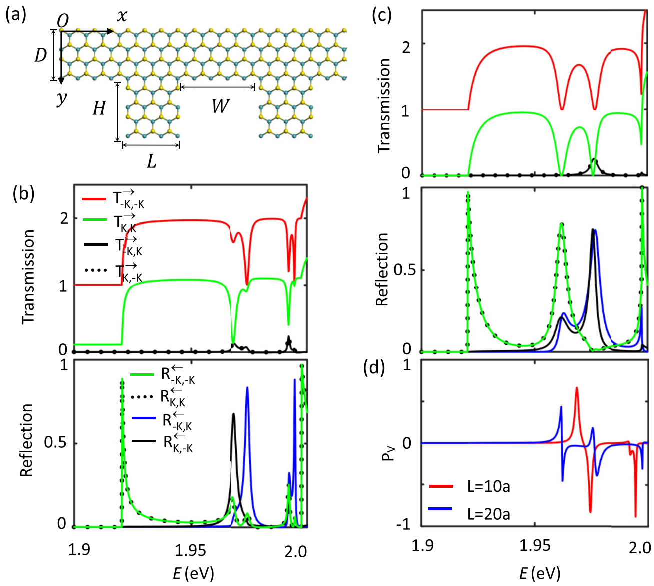

FIG. 1. Valley-resolved Fano resonance as electron transmission through a MTMD nanoribbon with an attached stub. (a) Schematic of nanoribbons with attached stubs connected to MTMD leads on the two sides. (b) Valley-resolved transmission and reflection coefficients as functions of the incident energy, with $L = 10a$, a being the lattice constant of MTMDs. (c) Valley-resolved transmission and reflection coefficients for $L = 20a$. (d) Valley polarization P_v of the transmission as a function of the incident energy for the two configurations. All calculations here use parameters $D = 10\sqrt{3}a$ and $H = 4\sqrt{3}a$ [cf. Fig. 1(a)].

be obtained when the electron incident energy is in these valley-resolved gaps even for a nanoribbon with several stubs attached.

II. MODEL AND METHODS

Let us consider a MTMD zigzag nanoribbon with attached stubs of length L and width H [Fig. 1(a)]. The width of the nanoribbon is D, and the spacing of the stubs is W. In MTMDs, the conduction edges at the $\pm K$ valleys are contributed predominantly by the three metal d orbitals [45]: d_{z^2}, d_{xy}, and $d_{x^2-y^2}$. For a quantitative characterization of the valley-polarized transport and superlattice minibands, with the Fano interference of intervalley backscattering, we have calculated the valley-dependent transport properties and energy dispersion using the tight-binding model constructed with the three orbitals that describes well the band edge electrons [45],

$$H = \sum_i \sum_\mu \varepsilon_{i\mu} c^\dagger_{i\mu} c_{i\mu} + \sum_{\langle i,j\rangle} \sum_{\mu\nu} t_{i\mu,j\nu} c^\dagger_{i\mu} c_{j\nu}. \tag{1}$$

Here, $\epsilon_{i\mu}$ and $c^\dagger_{i\mu}$ are the on-site energy and the creation operator, respectively, for the electron on orbital μ at metal site i, the sums $\langle i, j\rangle$ run over all pairs of nearest-neighbor metal sites, and $t_{i\mu,i\nu}$ are the hopping terms fitted from first-principles band structures [45].

Consider a nanoribbon with stubs connected to the outer world by left and right semi-infinite pristine MTMD leads; the valley-resolved transport properties of the system with the tight-binding Hamiltonian in Eq. (1) are calculated using a recursive Green's function technique [46] in Appendix A.

III. RESULTS AND DISCUSSION

As examples, we numerically demonstrate the sizable valley polarization effects driven by Fano resonance of intervalley backscattering in monolayer MoS_2 nanoribbons with stubs. The widths of the nanoribbon and the stub are set as $D = 10\sqrt{3}a$ and $H = 4\sqrt{3}a$, respectively, a being the lattice constant of MoS_2. Figure 1(b) shows the calculated valley-conserved and valley-flip transmission and reflection coefficients for a nanoribbon with one stub attached with $L = 10a$. The two valley-conserved reflection coefficients $R^{\leftarrow}_{K,K}$ and $R^{\leftarrow}_{-K,-K}$ are always identical, as they correspond to intravalley backscatterings with the same momentum transfers. The two valley-flip transmission coefficients are equal, i.e., $T^{\rightarrow}_{K,-K} = T^{\rightarrow}_{-K,K}$, as the two scattering channels are conjugates of each other [29]. Both of the valley-conserved transmission coefficients, $T^{\rightarrow}_{K,K}$ and $T^{\rightarrow}_{-K,-K}$ in Fig. 1(b), exhibit a wide plateau and a series of dips on the plateau. These dips arise from the Fano-type interference between the continuous states propagating in the main channel and a bound state formed in the stub. This type of resonance is called structure-induced Fano resonance. The peaks of valley-flip reflection coefficients in Fig. 1(b) indicate that the Fano resonance here is a quantum destructive interference behavior with strong intervalley backscattering. The valley-resolved Fano resonance of transmission coefficients in Fig. 1(b) is caused by the combined effect of intervalley backscattering and quantum interference.

The charge current passing through the nanoribbon with a stub is accompanied by a valley-polarized flow when the electron incident energy is set at the Fano resonant position. In order to study the valley polarization caused by Fano resonance with intervalley backscattering, we do not consider the effect of the edge state, because the valley-dependent transport properties of the edge state are obvious. At the upper boundary of the nanoribbon, the electrons in the $-K$ valley propagate steadily to the right lead and will not be affected by the stub [47]. At the bottom of the conduction band, the edge states propagating to the right belong only to the $-K$ valley. In any low-energy region, the contribution of edge states to transmission is always 1. Here, what we are concerned with is the contribution of bulk states to valley polarization, so we remove the edge state contribution. The valley polarization can be defined as $P_v \equiv \frac{1}{T}(T^{\rightarrow}_{K,K} + T^{\rightarrow}_{-K,K} - \widetilde{T}^{\rightarrow}_{-K,-K} - T^{\rightarrow}_{K,-K})$, where $\widetilde{T}^{\rightarrow}_{-K,-K} = T^{\rightarrow}_{-K,-K} - 1$ and $T = T^{\rightarrow}_{K,K} + T^{\rightarrow}_{-K,K} + \widetilde{T}^{\rightarrow}_{-K,-K} + T^{\rightarrow}_{K,-K}$ remove the edge state contribution. Figure 1(d) plots the valley polarization as a function of the incident energy for $L = 10a$ and $L = 20a$. A pronounced valley polarization almost reaching $\sim$85% can be obtained in nanoribbons with a short stub, for example, $L = 10a$, in which the intervalley backscattering results in significant valley-resolved Fano resonance. Moreover, the direction of valley polarization can be controlled by the incident energy.

We also examined the effect of the stub size on the Fano resonance. When the size of the stub increases, two kinds of Fano resonances appear on the transmission spectra plateau, as shown in Fig. 1(c). It can be seen from the reflection coefficients that one is mainly caused by intravalley backscattering and the other is induced by intervalley backscattering. The valley splitting effect of Fano resonance will be suppressed when the size of the stub increases. The valley-resolved Fano resonance positions are difficult to distinguish in terms of the incident energy. In this case, valley polarization is generated near the Fano resonance energy positions, but the strength of the valley polarization is reduced, as shown in Fig. 1(d).

In order to offer the most general guides for achieving the best result of the valley polarization, we can discuss the location of the dips in the transmission spectra. It depends on the energy levels in the stubs. An analytical expression for the spectral intensity was first proposed and later applied to an Aharonov-Bohm ring with an embedded quantum dot (QD-AB ring) [3] and T-shaped quantum waveguides [48],

$$T(\varepsilon) \propto \frac{(\varepsilon + q)^2}{\varepsilon^2 + 1}, \tag{2}$$

with $\varepsilon = \frac{E - E_0}{\Gamma/2}$, where E_0 and Γ are the energy position and width of the resonance state, respectively. The Fano parameter q is a measure of the coupling strength between the continuum state and the resonance state. The Fano parameter q selects from a symmetric peak ($q = \infty$) or dip ($q = 0$), or a dip to the left ($q > 0$) or right ($q < 0$) of a peak. Here, we can set $q = 0$ and roughly fit the dips in the transmission for the valley-resolved Fano resonance in Fig. 2(a). There are two kinds of intervalley scatterings with distinct momentum transfers [29]. In the first Born approximation, $R^{\leftarrow}_{K,-K}$ and $R^{\leftarrow}_{-K,K}$ simply correspond to different Fourier components of the scattering potential at $2K + 2q_F$ and $2K - 2q_F$, respectively, where q_F is the Fermi wave vector. Due to the quantum size effect, two kinds of intervalley scatterings lead to valley-resolved energy levels in the stub. According to Eq. (2), the valley-resolved energy levels distinguish the transmission in the two valleys at the energies of Fano resonance.

Figures 2(a) and 2(b) plot the total transmission, $T_{\rm sum} = T^{\rightarrow}_{K,K} + T^{\rightarrow}_{-K,K} + T^{\rightarrow}_{-K,-K} + T^{\rightarrow}_{K,-K}$, as a function of the incident energy for $L = 10a$ and $L = 20a$, respectively. In the bulk energy gap below the bottom of the conduction band, the total transmission $T_{\rm sum} = 1$ is the contribution of the edge state. For Fano resonance with intervalley backscattering, such as point D in Fig. 2(a), the quantum interference is not completely destructive, and one of the valleys is retained in the total transmission. For point F in Fig. 2(b), Fano resonance with intravalley backscattering is completely destructive quantum interference. It is pointed out that the Fano resonances are contributed by both intervalley and intravalley backscattering. For some resonance dips, one of them plays the dominant role. For example, point F in Fig. 2(b) corresponds to a resonance mainly due to intravalley backscattering, while point D in Fig. 2(a) is a resonance mostly contributed by intervalley backscattering. We have superimposed the relative contributions of intravalley backscattering and intervalley backscattering on the transmission spectrum to identify the two backscattering processes more easily, as shown in Figs. 2(a) and 2(b).

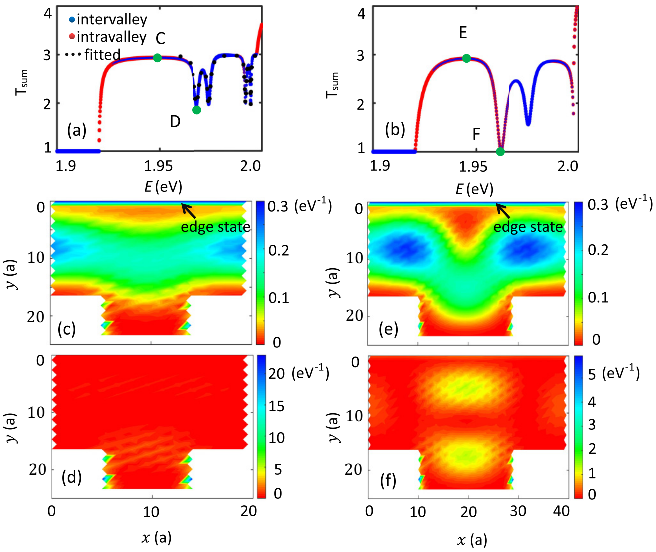

FIG. 2. Local density of states of MTMD nanoribbons with a stub. (a) The total transmission and fits (black dotted line) as a function of the incident energy for $L = 10a$. Blue and red dots represent intervalley and intravalley backscattering, respectively, and the size of the dots represents the contribution to the total transmission. (b) The total transmission for $L = 20a$. (c)–(d) Profiles of the local density of states as the incident energies are taken at the positions marked by the four corresponding green points (points C, D, E, and F) shown in (a) and (b). Black arrows indicate edge states in (c) and (e).

In order to understand the localized state distribution in the stub which causes the valley splitting effect of Fano resonance in detail, in Figs. 2(c)–(f) we plot the profiles of the local state density of the system at different electron incident energies denoted by the four green points in Figs. 2(a) and 2(b). The edge state at the upper boundary of the nanoribbon will not be destroyed by the stub at any incident energy shown in Figs. 2(c)–(f). When the electron incident energy is set in the transmission plateau region, there are no localized states in the stub, and the electron is perfectly transmitted through the continuous states in the nanoribbon, as Fig. 2(c) illustrates. As can be seen from the profile of the local state density at point E in Fig. 2(e), when the stub length increases, the continuous channels in the nanoribbon shift to the stub, but the electron is still not localized by the stub.

At the intervalley-backscattering Fano resonant energy positions, such as point D, the electrons are sharply localized on the left and right boundaries of the stub. The distribution range of the local states can be compared with the lattice constant of the MTMDs, so there is a significant intervalley backscattering effect during electron transmission. It is the localized states on the armchair boundary of the stub that give rise to valley-polarized Fano resonance. As shown in Fig. 2(f), for the incident energy corresponding to the energy position of Fano resonance mainly induced by intravalley backscattering, the local state density is highly localized inside the stub region and forms two isolated islands. In this situation, standing waves are formed by the interference between the electron

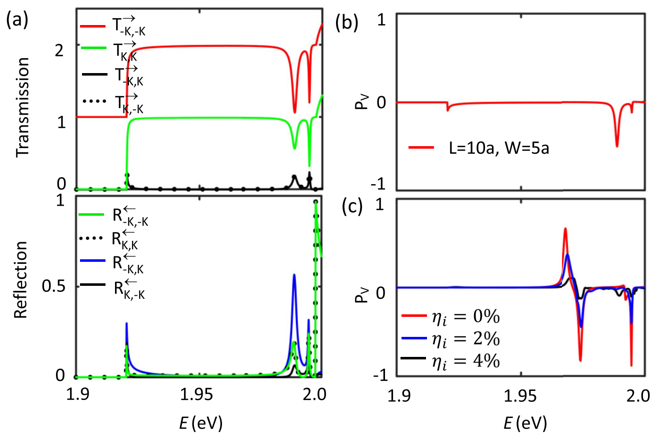

FIG. 3. The effects of different edges and defects on the valley-resolved Fano resonance. (a) Valley-resolved transmission and reflection coefficients as functions of the incident energy for a stub with left and right zigzag edges, with $L = 10a$ and $W = 5a$. (b) Valley polarization as a function of the incident energy for a stub with zigzag edges. (c) Valley polarization as a function of the incident energy for various defect densities η_i in the stub.

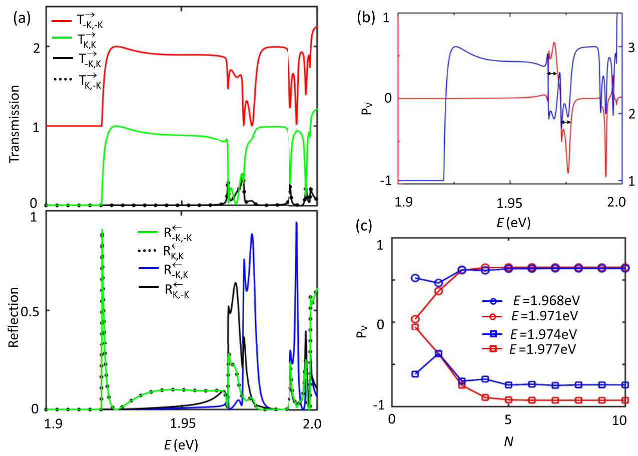

FIG. 4. Valley-polarized transmission through a MTMD nanoribbon with multiple stubs. (a) Valley-resolved transmission and reflection coefficients as functions of the incident energy for two stubs, with $L = 10a$ and $W = 5a$. (b) The corresponding valley polarization and the total transmission as functions of the incident energy. (c) Valley polarization as a function of the number of stubs for various incident energies in the region indicated by double-headed arrows in (b).

waves reflected from the walls of the stub and those in the nanoribbon.

Figures 3(a) and 3(b) show the Fano resonance and the resultant valley polarization when the left and right boundaries of the stub are zigzag edges. It is found that the valley splitting effect of Fano resonance is suppressed in this case. The reason is that the intervalley scattering is not significant in the stub with zigzag edges, so the valley-resolved energy level splitting is weakened. Therefore the armchair edge of the stub is one of the important factors in obtaining high valley polarization. Figure 3(c) shows the valley polarization as a function of the incident energy for various defect densities η_i in the stub. Although the location of the dips remained the same, the strength of the dips became weaker. Valley polarization decreases with the increase in defect density in the stub area.

The sharpness of the valley-polarized Fano resonances is limited to valley filtering applications, so we also studied the effect of the number of stubs on the valley-polarized transport properties. Figure 4(a) shows the calculated valley-conserved and valley-flip transmission and reflection coefficients for a two-stub nanoribbon with $L = 10a$ and $W = 5a$. Each valley-polarized Fano resonance dip is split into two, which broadens the range of the incident energy for valley polarization. Each valley polarization peak of the nanoribbon with one stub becomes two peaks now, and the valley polarization maintains a high intensity in a certain incident energy range, as shown in Fig. 4(b). If the number of stubs attached to the nanoribbon continues to increase, the valley-polarized Fano resonance dips, and the valley polarization peaks split further into more dips and peaks. Figure 4(c) shows the valley polarization as a function of the number of stubs when the incident energy is in the energy range indicated by the double-headed arrows in Fig. 4(b). Large valley polarization is obtained over a wide energy range, and remarkably, by just using four stubs, the valley polarization can already reach ~60-90% [cf. Fig. 4(c)].

According to the superlattice transport theory, as long as the distance between the stubs is not too far and the wave functions in the adjacent stubs can overlap, a nanoribbon with multiple stubs will have the properties of miniband transport; that is, the system will have valley-resolved minibands and minigaps. Figure 5(a) shows an example of the stub superlattice energy bands, with $L = 10a$ and $W = 5a$, where the length of the supercell is $L + W$. In the superlattice, the edge states still exist perfectly [indicated by the arrows in Fig. 5(a)], and zone folding does not open the energy gap in the edge states, because the edge states cannot be reflected by the stubs. Our calculation finds that the strong intravalley backscattering shown in Fig. 5(d) leads to a sizable bulk minigap Δ at the boundary of the minizone.

Besides the bulk minigap Δ, there are two valley-resolved minigaps Δ_+ and Δ_- at the center and boundary of the minizone, respectively. In the neighborhood of Δ_+ and Δ_-, multiple intervalley backscatterings by the stubs give rise to closely spaced Fano resonance dips which will develop into minigaps in an infinite-period superlattice. Within the gaps Δ_+ and Δ_-, the minibands are valley polarized. The Fano resonance with intervalley backscattering makes possible energy windows for valley-polarized transport in the superlattice. Figures 5(b) and 5(c) show the valley polarization and transmission as functions of the incident energy, for a 20-stub superlattice with $L = 10a$ and $W = 5a$. As the periods increase, the Fano resonance dips in transmission are further split into groups of valley-resolved dips. These dips evolve into continuous valley-resolved minigaps in the limit of a superlattice. This leads to a pronounced valley polarization exceeding 90%, with a total transmission $T_{\text{sum}} \sim 2$ [Fig. 5(b)]. If the valley polarization is defined by the conductance, the transmission coefficient should be weighted by the Fermi distributions of the leads and integrated over energy. The valley imbalance regarding the carrier densities achieved by

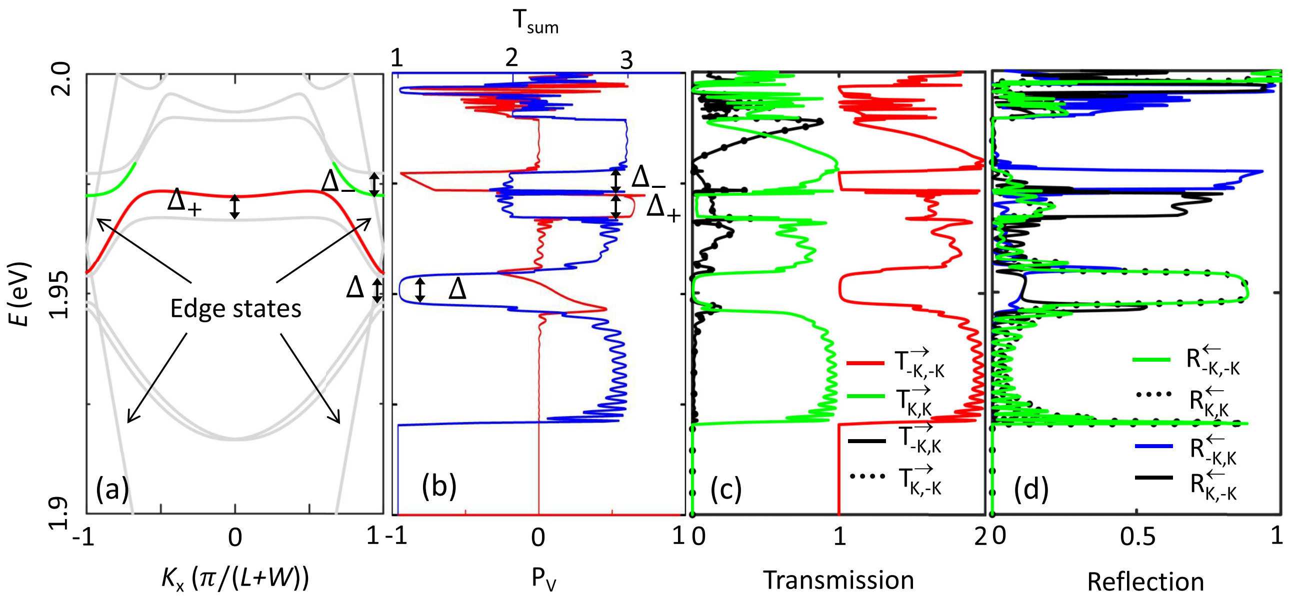

FIG. 5. Valley filtering performance for the stub superlattice. (a) An example of superlattice miniband dispersion, with $L = 10a$ and $W = 5a$. The lines indicated by the arrows are the edge states of the system. In the case of zone folding, intravalley backscattering causes a bulk minigap Δ at the boundary of the minizone. The intervalley backscattering gives rise to two valley-resolved gaps Δ_+ and Δ_- at the center and boundary of the minizone, respectively. The upper of the two bands split by Δ_+ is responsible for the transmission of the $-K$ valley state, which is colored in red. The lower of the two bands split by Δ_- is responsible for the transmission of the K valley state, which is colored in green. (b) Valley polarization and transmission as functions of the incident energy. (c) Valley-resolved transmission coefficients. (d) Valley-resolved reflection coefficients. The number of superlattice periods $N = 20$ is used in (b)–(d).

the valley filter may be significantly diluted due to the valley-resolved gaps being narrow and adjacent to each other.

IV. CONCLUSIONS

In summary, we have shown that a remarkable valley filtering can be realized in a MTMD nanoribbon with attached stubs due to the Fano resonance with the intervalley backscattering. The edge states on the boundaries of the stub and the bulk localized states in the stubs cause the intervalley- and intravalley-backscattering Fano resonance, respectively. It is the intervalley-backscattering Fano resonance that results in a significant valley polarization. The valley-resolved Fano resonance will split when the number of stubs increases, and the valley-resolved minigaps are formed at the supercell Brillouin zone boundary and center for the stub superlattice structure. The transmission has nearly perfect valley polarization in these gaps with alternating valley polarity. This broadens the valley-polarized energy region and makes possible control of the valley filtering functionality by electrostatic control. Moreover, a valley polarization in a wide energy region can be generated in nanoribbons with just a few stubs. These results point to an unexpected but exciting opportunity to build valley functionality by quantum interference in a MTMD nanostructure.

ACKNOWLEDGMENTS

This work was supported by the National Natural Science Foundation of China (Grant No. 12074096) and Hebei Province Natural Science Foundation of China (Grant No. A2021208013).

APPENDIX A: RECURSIVE GREEN'S FUNCTION TECHNIQUE

In the main text, we used the recursive Green's function method, which is very convenient in solving quantum transport. This method is utilized in the calculation of valley pump of electrons or holes at nonmagnetic disorders [29]. Here, we derive the recursive Green's function method. We assume that for each unit cell with an index i, the equation of motion can be written as

$$-(E\boldsymbol{I} - \boldsymbol{H}_i)\boldsymbol{C}_i + \boldsymbol{H}_{i,i-1}\boldsymbol{C}_{i-1} + \boldsymbol{H}_{i,i+1}\boldsymbol{C}_{i+1} = 0, \tag{A1}$$

where $\boldsymbol{C}_i$ is a vector describing the wave-function coefficients on all sites and orbits of unit cell i within the three-band tight-binding model. The matrices $\boldsymbol{H}_i$ and $\boldsymbol{H}_{i,i+1}$ consist of the unit cell and hopping matrix of the Hamiltonian, respectively. The equation of motion can be rewritten in transfer matrix form:

$$\begin{pmatrix} \boldsymbol{C}_{i+1} \\ \boldsymbol{C}_i \end{pmatrix} = \begin{pmatrix} \boldsymbol{H}_{i,i+1}^{-1}(E\boldsymbol{I} - \boldsymbol{H}_i) & -\boldsymbol{H}_{i,i+1}^{-1}\boldsymbol{H}_{i,i-1} \\ \boldsymbol{I} & 0 \end{pmatrix} \otimes \begin{pmatrix} \boldsymbol{C}_i \\ \boldsymbol{C}_{i-1} \end{pmatrix}. \tag{A2}$$

We suppose the solutions of Eq. (A2) to have Bloch symmetry, $\boldsymbol{C}_i = \lambda\boldsymbol{C}_{i-1}$ and $\boldsymbol{C}_{i+1} = \lambda^2\boldsymbol{C}_{i-1}$. Substituting this into Eq. (A2) results in an eigenvalue problem,

$$\begin{pmatrix} \boldsymbol{H}_{i,i+1}^{-1}(E\boldsymbol{I} - \boldsymbol{H}_i) & -\boldsymbol{H}_{i,i+1}^{-1}\boldsymbol{H}_{i,i-1} \\ \boldsymbol{I} & 0 \end{pmatrix} \begin{pmatrix} \boldsymbol{C}_i \\ \boldsymbol{C}_{i-1} \end{pmatrix} = \lambda \begin{pmatrix} \boldsymbol{C}_i \\ \boldsymbol{C}_{i-1} \end{pmatrix}. \tag{A3}$$

The eigenvalue λ is related to the wave vector k through $\lambda = \exp(ika)$. The eigenvalues are denoted by $\lambda_n(\pm)$, and the corresponding eigenvectors are denoted by $\boldsymbol{u}_n(\pm)$, where the right-going and left-going modes are labeled as $(+)$ and $(-)$. The Bloch velocities are given by the expression

$$v_n(\pm) = -\frac{2a}{\hbar}\,\mathrm{Im}[\lambda_n(\pm)\boldsymbol{u}_n^\dagger(\pm)H_{i,i+1}^\dagger\boldsymbol{u}_n(\pm)]. \tag{A4}$$

Define

$$\boldsymbol{U}(\pm) = (\boldsymbol{u}_1(\pm)\cdots\boldsymbol{u}_{3N_y}(\pm)) \tag{A5}$$

and

$$\Lambda(\pm) = \begin{pmatrix} \lambda_1(\pm) & & \\ & \ddots & \\ & & \lambda_{3N_y}(\pm) \end{pmatrix}, \tag{A6}$$

where N_y is the number of metal atoms in the y direction; then we have

$$\boldsymbol{F}(\pm) = \boldsymbol{U}(\pm)\boldsymbol{\Lambda}(\pm)\boldsymbol{U}^{-1}(\pm). \tag{A7}$$

The transmission coefficient for the incident mode m with velocity v_m and outgoing mode n with velocity v_n can be obtained as

$$t_{mn} = \sqrt{\frac{v_n}{v_m}}\{-\boldsymbol{U}^{-1}(+)G_{N_x+1,0}\boldsymbol{H}_{0,-1} \otimes[\boldsymbol{F}^{-1}(+) - \boldsymbol{F}^{-1}(-)]\boldsymbol{U}(+)\}_{mn}, \tag{A8}$$

and the reflection coefficient for the incident mode m and outgoing mode n can be obtained as

$$r_{mn} = \sqrt{\frac{v_n}{v_m}}(\boldsymbol{U}^{-1}(-)\{-\boldsymbol{G}_{0,0}\boldsymbol{H}_{0,-1} \otimes[\boldsymbol{F}^{-1}(+) - \boldsymbol{F}^{-1}(-)] - \boldsymbol{I}\}\boldsymbol{U}(+))_{mn}. \tag{A9}$$

Here, N_x is the number of metal atoms in the x direction, and the Green's function matrix block $\boldsymbol{G}_{N_x+1,0}$ and $\boldsymbol{G}_{0,0}$ can be found using a set of recursive formulas [46]. Therefore the valley-dependent transmission and reflection coefficients for the incident valley A and outgoing valley A' ($A, A' = K$ or $-K$) can be defined as

$$T_{A',A} = \sum_{m\in\{A'\},\, n\in\{A\}} |t_{mn}|^2 \tag{A10}$$

and

$$R_{A',A} = \sum_{m\in\{A'\},\, n\in\{A\}} |r_{mn}|^2, \tag{A11}$$

respectively.

APPENDIX B: BAND STRUCTURE

In quantum transport theory, there are often multiple modes in the system involved in transport. For each mode m, its transmission coefficient $\sum_n |t_{mn}|^2$ in Eq. (A10) is always between 0 and 1. For transmission of multiple modes, in order to distinguish the contribution of each mode to the transmission, the usual practice is to sum the transmission coefficient of each mode, $\sum_{m,n} |t_{mn}|^2$, as the transmission coefficient for all modes. Therefore the transmission here is greater than 1. If

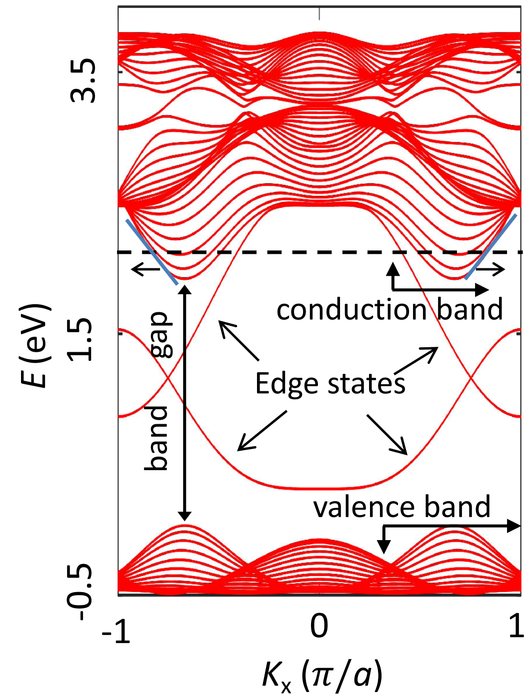

FIG. 6. The band structure of a nanoribbon without stubs. Black arrows mark valence bands, conduction bands, edge states, and the band gap. The black dashed line represents the Fermi level, the number of the subbands passing through the Fermi level is the number of modes involved in transport, and the "left-going" and "right-going" directions of the group velocity for the states at Fermi energy are determined by the slope of the dispersion. The short blue line shows the tangent line of the dispersion, which is represented by "$\rightarrow$" when the slope is greater than 0 and "$\leftarrow$" when the slope is less than 0. "$\rightarrow$" and "$\leftarrow$" represent the direction of movement to the left and right, respectively.

we assume that each mode in the left lead has an incident electron, the transmission coefficient we calculated divided by the number of modes will be approximately between 0 and 1.

For monolayer two-dimensional (2D) MoS_2, in both the K and $-K$ valleys, there could be electrons going along all directions in the 2D plane. Here, we study a monolayer MoS_2 nanoribbon. For finite-width nanoribbons, due to quantum size effects, the two-dimensional band becomes a series of subbands, as shown in Fig. 6. The band gap indicated by the double-headed arrow is approximately 1.8 eV, and the black dashed line represents the Fermi level. The number of subbands passing through the Fermi level is the number of modes involved in transport. When the energy E is between 1.9 and 1.92 eV, only the edge state passes through the Fermi level, which is a single-mode transport. It can be found that in Fig. 1(b), when E is between 1.9 and 1.92 eV, the transmission is between 0 and 1; meanwhile, in Fig. 2(a), when E is between 1.9 and 1.92 eV, the total transmission is between 0 and 1. In Fig. 1(b), the value of $T_{-K,-K}^{\rightarrow}$ is greater than 2, indicating that more than two modes are involved in the transport of the $-K$ valley.

The band structure in Fig. 5(a) could be understood by folding the one in Fig. 6 with the effect of the coupling with the stub. The Brillouin zone folding leads to intersections of bands. At the intersection points of bands of propagating right in the K valley and propagating left in the $-K$ valley, the intervalley-backscattering $R^{\leftarrow}_{K,-K}$ gives rise to the $-K$-valley-polarized gap Δ_+. In contrast, the intervalley-backscattering $R^{\leftarrow}_{-K,K}$ results in the K-valley-polarized gap Δ_- at the intersection points of bands of propagating right in the $-K$ valley and propagating left in the K valley.

In the quantum confinement direction, we have no way to define the group velocity. According to the definition of group velocity, $v = \frac{1}{\hbar}\frac{\partial E}{\partial k}$, the "left-going" and "right-going" directions of the group velocity for the states at Fermi energy are determined by the slope of the dispersion. "→" and "←" represent the direction of movement to the left and right, respectively.

---

[1] U. Fano, Phys. Rev. **124**, 1866 (1961).
[2] E. Tekman and P. F. Bagwell, Phys. Rev. B **48**, 2553 (1993).
[3] K. Kobayashi, H. Aikawa, S. Katsumoto, and Y. Iye, Phys. Rev. Lett. **88**, 256806 (2002).
[4] A. C. Johnson, C. M. Marcus, M. P. Hanson, and A. C. Gossard, Phys. Rev. Lett. **93**, 106803 (2004).
[5] D. Sánchez and L. Serra, Phys. Rev. B **74**, 153313 (2006).
[6] P. Recher, B. Trauzettel, A. Rycerz, Y. M. Blanter, C. W. J. Beenakker, and A. F. Morpurgo, Phys. Rev. B **76**, 235404 (2007).
[7] F. Zhai and H. Q. Xu, Phys. Rev. B **76**, 035306 (2007).
[8] M. P. Nowak, B. Szafran, and F. M. Peeters, Phys. Rev. B **84**, 235319 (2011).
[9] C.-R. Liu, L. Huang, H. Luo, and Y.-C. Lai, Phys. Rev. Appl. **13**, 034061 (2020).
[10] Y. Q. Huang, J. Beyer, Y. Puttisong, I. A. Buyanova, and W. M. Chen, Phys. Rev. Lett. **127**, 127401 (2021).
[11] M. D. Petrović and F. M. Peeters, Phys. Rev. B **91**, 035444 (2015).
[12] M. Amini, M. Soltani, and M. Sharbafiun, Phys. Rev. B **99**, 085403 (2019).
[13] F. Borsoi, K. Zuo, S. Gazibegovic, R. L. M. Op Het Veld, E. Bakkers, L. P. Kouwenhoven, and S. Heedt, Nat. Commun. **11**, 3666 (2020).
[14] W. Wang, Y. Jin, W. Wang, B. Bonello, B. Djafari-Rouhani, and R. Fleury, Phys. Rev. B **101**, 024101 (2020).
[15] K. Nikolić and R. Šordan, Phys. Rev. B **58**, 9631 (1998).
[16] P. Fan, Z. Yu, S. Fan, and M. L. Brongersma, Nat. Mater. **13**, 471 (2014).
[17] B. Lee, J. Park, G. H. Han, H. S. Ee, C. H. Naylor, W. Liu, A. T. Johnson, and R. Agarwal, Nano Lett. **15**, 3646 (2015).
[18] N. Myoung, J.-W. Ryu, H. C. Park, S. J. Lee, and S. Woo, Phys. Rev. B **100**, 045427 (2019).
[19] M. Wang, A. Krasnok, T. Zhang, L. Scarabelli, H. Liu, Z. Wu, L. M. Liz-Marzán, M. Terrones, A. Alù, and Y. Zheng, Adv. Mater. (Weinheim) **30**, 1705779 (2018).
[20] A. Rycerz, J. Tworzydło, and C. W. J. Beenakker, Nat. Phys. **3**, 172 (2007).
[21] N. Singh and U. Schwingenschlögl, Adv. Mater. (Weinheim) **29**, 1600970 (2017).
[22] D. Gunlycke and C. T. White, Phys. Rev. Lett. **106**, 136806 (2011).
[23] Y. Wang, L. Deng, Q. Wei, Y. Wan, Z. Liu, X. Lu, Y. Li, L. Bi, L. Zhang, H. Lu, H. Chen, P. Zhou, L. Zhang, Y. Cheng, X. Zhao, Y. Ye, W. Huang, S. J. Pennycook, K. P. Loh, and B. Peng, Nano Lett. **20**, 2129 (2020).
[24] T. Low and F. Guinea, Nano Lett. **10**, 3551 (2010).
[25] N. Myoung, H. Choi, and H. C. Park, Carbon **157**, 578 (2020).
[26] Z. Wu, F. Zhai, F. M. Peeters, H. Q. Xu, and K. Chang, Phys. Rev. Lett. **106**, 176802 (2011).
[27] A. Georgi, P. Nemes-Incze, R. Carrillo-Bastos, D. Faria, S. V. Kusminskiy, D. Zhai, M. Schneider, D. Subramaniam, T. Mashoff, N. M. Freitag, M. Liebmann, M. Pratzer, L. Wirtz, C. R. Woods, R. V. Gorbachev, Y. Cao, K. S. Novoselov, N. Sandler, and M. Morgenstern, Nano Lett. **17**, 2240 (2017).
[28] S. Y. Li, Y. Su, Y. N. Ren, and L. He, Phys. Rev. Lett. **124**, 106802 (2020).
[29] X.-T. An, J. Xiao, M. W.-Y. Tu, H. Yu, V. I. Fal'ko, and W. Yao, Phys. Rev. Lett. **118**, 096602 (2017).
[30] X.-T. An and W. Yao, Phys. Rev. Appl. **14**, 014039 (2020).
[31] H. Yu, Y. Wu, G.-B. Liu, X. Xu, and W. Yao, Phys. Rev. Lett. **113**, 156603 (2014).
[32] M. Sui, G. Chen, L. Ma, W.-Y. Shan, D. Tian, K. Watanabe, T. Taniguchi, X. Jin, W. Yao, D. Xiao, and Y. Zhang, Nat. Phys. **11**, 1027 (2015).
[33] K. F. Mak, K. L. McGill, J. Park, and P. L. McEuen, Science **344**, 1489 (2014).
[34] K. Komatsu, Y. Morita, E. Watanabe, D. Tsuya, K. Watanabe, T. Taniguchi, and S. Moriyama, Sci. Adv. **4**, eaaq0194 (2018).
[35] P. Back, M. Sidler, O. Cotlet, A. Srivastava, N. Takemura, M. Kroner, and A. Imamoglu, Phys. Rev. Lett. **118**, 237404 (2017).
[36] Y. Ye, J. Xiao, H. Wang, Z. Ye, H. Zhu, M. Zhao, Y. Wang, J. Zhao, X. Yin, and X. Zhang, Nat. Nanotechnol. **11**, 598 (2016).
[37] D. Zhong, K. L. Seyler, X. Linpeng, R. Cheng, N. Sivadas, B. Huang, E. Schmidgall, T. Taniguchi, K. Watanabe, M. A. McGuire, W. Yao, D. Xiao, K.-M. C. Fu, and X. Xu, Sci. Adv. **3**, e1603113 (2017).
[38] P. Nagler, M. V. Ballottin, A. A. Mitioglu, F. Mooshammer, N. Paradiso, C. Strunk, R. Huber, A. Chernikov, P. C. M. Christianen, C. Schuller, and T. Korn, Nat. Commun. **8**, 1551 (2017).
[39] Q. Li, X. Zhao, L. Deng, Z. Shi, S. Liu, Q. Wei, L. Zhang, Y. Cheng, L. Zhang, H. Lu, W. Gao, W. Huang, C. W. Qiu, G. Xiang, S. J. Pennycook, Q. Xiong, K. P. Loh, and B. Peng, ACS Nano **14**, 4636 (2020).
[40] L. Li, S. Jiang, Z. Wang, K. Watanabe, T. Taniguchi, J. Shan, and K. F. Mak, Phys. Rev. Materials **4**, 104005 (2020).
[41] C. Zhang, Y. Nie, S. Sanvito, and A. Du, Nano Lett. **19**, 1366 (2019).
[42] T. Smoleński, M. Goryca, M. Koperski, C. Faugeras, T. Kazimierczuk, A. Bogucki, K. Nogajewski, P. Kossacki, and M. Potemski, Phys. Rev. X **6**, 021024 (2016).
[43] D. Xiao, G.-B. Liu, W. Feng, X. Xu, and W. Yao, Phys. Rev. Lett. **108**, 196802 (2012).

[44] W. Yao, D. Xiao, and Q. Niu, Phys. Rev. B **77**, 235406 (2008).
[45] G.-B. Liu, W.-Y. Shan, Y. Yao, W. Yao, and D. Xiao, Phys. Rev. B **88**, 085433 (2013).
[46] T. Ando, Phys. Rev. B **44**, 8017 (1991).
[47] A. Sekine and A. H. MacDonald, Phys. Rev. B **102**, 155205 (2020).
[48] S. Klaiman, N. Moiseyev, and H. R. Sadeghpour, Phys. Rev. B **75**, 113305 (2007).